Y. Feng et al.

On the W7-X divertor performance under detachment conditions

Preprint of Paper to be submitted for publication in
Nuclear Fusion

On the W7-X divertor performance under detachment conditions

Y. Feng, C. D. Beidler, J. Geiger, P. Helander, H. Hölbe, H. Maassberg, Y. Turkin

Max-Planck-Institute for Plasma Physics, 17491 Greifswald, Germany

D. Reiter

Forschungszentrum Jülich GmbH, Institut für Energie- und Klimaforschung
– Plasmaphysik, 52425 Jülich, Germany

Abstract

We present a theoretical/numerical predictive analysis of the W7-X island divertor performance under condition of detachment characterized by intensive radiation. The analysis is based on EMC3-Eirene simulations and the earlier W7-AS experimental and numerical experience. Carbon is employed as a representative radiator. The associated drawbacks, i.e. core contamination and recycling degradation (reduced recycling flux), are evaluated by measuring the carbon density at the last closed flux surface (LCFS) and the neutral pressure in the divertor chamber. Optimum conditions are explored in both configuration and plasma parameter space. This study aims to identify the key geometric/magnetic and plasma parameters that affect the performance of detached plasmas in W7-X. In particular it is interested in questions such as what is expected when the islands are enlarged far beyond the maximum size available in W7-AS and whether and in what sense there is an island size limit for optimal detachment operation, and why. Further issues addressed are the power removal ability of the W7-X edge islands, potentially-limiting factors, compatibility between particle and power exhaust and particle refueling capability of the recycling neutrals.

1. Introduction

Divertor experience gathered from tokamaks and stellarators so far strongly indicates that, on the way to a reactor, a strategy must be developed to remove most of the thermal power from the scrape-off layer (SOL) before it reaches solid surfaces [1-7]. For this purpose, radiation via light impurities is a concept that is intensively being explored across the world, both experimentally and theoretically [8, 9]. Thus, the reactor-relevance of a divertor concept is largely determined by its performance in a state of detachment characterized by enhanced radiation and reduced recycling flux. Here, the most critical issues are the particle-exhaust efficiency under reduced recycling flux conditions, impurity control under intense radiation, the stability of the detached state against thermal collapse in stellarators or current disruptions in tokamaks, and the maximum power removal capability of the divertor, including possible limiting factors.

Divertor experiments on tokamaks have shown that the X-point geometry favors radiation of light impurities to facilitate transition to detachment [10, 11, 12]. In comparison to the conventional poloidal divertor of tokamaks, which is axisymmetric and can be operated with single- or double-null, the island divertor for the low-shear W7-AS and W7-X stellarators [13, 14] is helically resonant and exhibits a multi-X-point geometry, depending on the poloidal mode number of the low-order island chain available at the edge. In the advanced low-shear W7-stellarators low-order magnetic islands are a natural product of the three-dimensionally (3D) shaped coils [15]. Nevertheless, first island divertor experiments on W7-AS with the ᵼ=5/9 island chain have shown that the inherent diverting fields are too weak to

stabilize detached plasmas against thermal instabilities [16]. Stable partial detachment operation was achieved by adding external resonant magnetic perturbation (RMP) fields through the so-called island control coils (similar to the RMP-coils recently introduced on tokamaks for controlling ELMs [17]). Analogously, in the helical divertor [18] of LHD stable detachment is achieved by introducing an external 1/1 RMP field component [19]. For stable partial detachment discharges in W7-AS, EMC3-Eirene simulations show that carbon radiation is concentrated at inner X-points [20]. A radially-thin, poloidally-modulated and helically-structured radiation layer/sheet is formed on the inboard side. By raising the plasma density the radiation layer moves inward and in the meanwhile poloidally shrinks toward the mid-plane. Once the radiation layer enters the confinement region, an intense radiation zone is formed around the inboard mid-plane [20], which is also observed experimentally [21, 22]. In this case, the plasma becomes unstable. Similar phenomena have also been observed in tokamaks and are known as MARFE (multifaceted asymmetric radiation from the edge) in the literature [23, 24, 25]. The fact that the inboard side favors MARFE formation in tokamaks is attributed to the enhanced heat source entering the SOL on the outboard side [26]. This hypothesis also explains the W7-AS results and is supported by the thermographic detection of a remnant hotspot on the target location magnetically closer to the outboard side during the stable detachment phase [16]. Associated with the in-out asymmetry in radiation, the maximum carbon radiation fraction achievable in simulations is below 80% [20]. In spite of the similar tendencies in the leading-order effects shown by experiment and modeling on W7-AS, there still remain numerous experimental details which numerically are not yet accessible. For example, asymmetries in divertor plasmas between the top and bottom divertor modules and among the strike zones as well are usually observed, especially in detachment [16, 27]. The asymmetries correlate with the B-field direction and thus are considered to be driven by classical drifts. A self-consistent treatment of the drifts is beyond the present code capability. The major experimental and theoretical achievements on the W7-AS island divertor can be found in [28, 29].

In comparison to W7-AS, W7-X has much bigger islands not only because of the increased machine size, but also because of a larger rotational transform and thereby reduced poloidal mode number of the edge islands. The W7-X divertor can be operated with ᵼ=5/6, 5/5 or 5/4 island chains, with the 5/5 island configuration termed as "standard". As a consequence, the poloidal extension of the W7-X islands is almost one order of magnitude larger than that of W7-AS. Previous EMC3-Eirene calculations in the absence of impurities have shown significant differences in divertor transport behavior between W7-AS and W7-X [7, 30]. In this paper we present a systematic numerical study of the island divertor behavior of W7-X under detachment conditions.
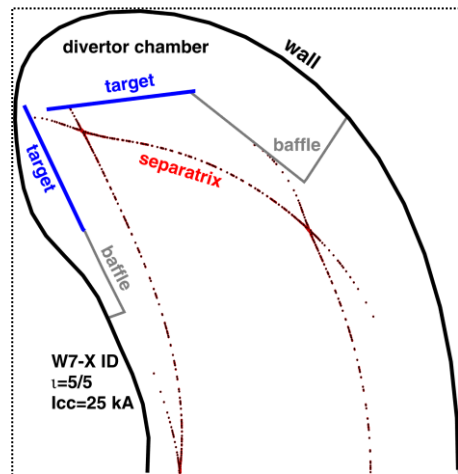

Fig.1: Cross-section of standard divertor configuration (SDC created by equal non-planar coil current) of W7-X at a bean-shaped plane. Targets and baffles form a closed chamber for neutral compression, with a gap opened between the two target plates to trap the recycling neutrals.

The aim is to identify the optimum conditions for detachment operation in both configuration and plasma parameter space, and potentially critical issues to be examined in the island divertor experiment starting soon on W7-X.

The paper is organized as follows. After introducing the W7-X island divertor in the next section, we define the boundary conditions of our studies in section 3. Section 4 then deals with the role of external perturbation fields. Island-size effects are addressed in section 5. Possible limiting factors are discussed in section 6. In section 7 we examine the favorable plasma density range for detachment operation. Island screening effects on the recycling neutrals are presented in section 8. The major results are summarized in section 9.

2. The W7-X island divertor

W7-X follows the island divertor concept tested on W7-AS. Ten identical divertor modules consisting of target and baffle plates are up/down-symmetrically installed around the bean-shaped planes, preserving the five-fold periodicity and stellarator symmetry of the machine [14]. In order not to restrict the operational configuration flexibility of W7-X, the divertor plates are not optimized with respect to any specific configuration. Rather, they are shaped to meet the basic flux surface form of W7-X constrained by the 3D coils so that the targets can effectively limit the plasma even in the absence of edge islands. The low-order resonances falling into the divertor operational ι-range are ι=5/6, 5/5 and 5/4 island chains, with the ι=5/5 one being the standard case. Figure 1 shows the poloidal cross-section of the standard divertor configuration in a bean-shape plane. Here, the so-called "standard" divertor configuration (SDC) is created by equal non-planar coil currents without planar coil contributions. The two targets indicated in figure 1 define the main plasma-surface interaction (PSI) for the ι=5/6 and 5/5 islands. The baffle plates are introduced to prevent the recycling neutrals from escaping from the recycling zone into the main chamber. The target and baffle plates, and the wall behind them, form a closed divertor chamber with a gap between the two target plates for trapping the recycling neutrals. The gap width varies in the toroidal direction. For the high-ι (5/4) case, the PSI region moves toroidally away from the bean-shaped plane to a toroidal location where only one horizontal target plate is installed and the divertor gap is small due to the limited space. The reduced opening has a negative consequence on the neutral compression in the divertor chamber, making particle pumping more difficult. Moving to the low-ι (5/6) case, the configuration becomes fatter, raising the risk of heat load on the baffle plates which have a poor power-handling capability. For these reasons we restrict our studies to the 5/5 island chain in this paper.

As on W7-AS, ten saddle coils, called "island control coils", are installed inside the vacuum vessel of W7-X for adjusting the island geometry externally. Sometimes they are also called "sweep coils", according to their original design function for sweeping strike lines. Nevertheless, the sweeping function has never been tested and how strongly the SOL and core plasma will be disturbed by this action is still an open question. On the other hand, island-divertor experiments on W7-AS have demonstrated their crucial importance in stabilizing detached plasmas, motivating a detailed analysis of their role in W7-X.

Because of the low shear, the location of the rational surface on which the divertor islands reside is sensitive to plasma currents [31]. The most critical one is the bootstrap current. In the absence of a transformer in W7-X, two strategies are being discussed for reducing the finite
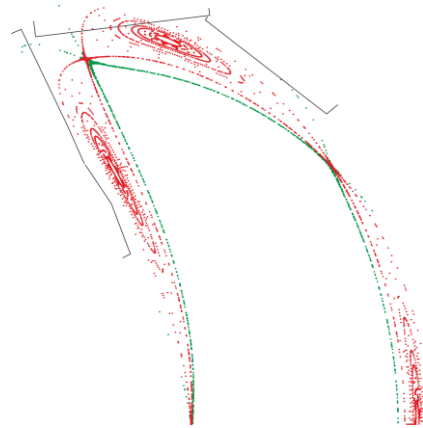
bootstrap current effects. First, current drive like ECCD can be applied to compensate the bootstrap current effects [32]. Second, specific configurations can be chosen that intrinsically have small bootstrap current, e.g. the high-mirror configuration. The former is an active method, facing the difficulties of a modified ɩ-profile in the confinement region and of low current drive efficiency at high densities. The latter method is passive and obviously restricts the operational configuration range of the device.

Associated with the stability issues given above, a precise positioning of the strike lines on the targets is experimentally difficult, in particular during dynamic phases before the plasma reaches a steady state. In order to avoid possible thermal damage of the edge tiles at the divertor gap side, it has been planned to install additional thermal-shielding plates called "scraper elements" outside the divertor module. Their thermal-shielding function and drawbacks on neutral compression have been assessed in [33]. They are not taken into account in the computations presented in this paper.

3. Boundary conditions

We employ the EMC3-Eirene code [34, 35]. EMC3 deals with a fluid model for electrons and ions and includes a trace impurity model. It solves a set of stationary fluid equations of Braginskii for continuity, parallel momentum and electron and ion energy transport. Parallel transport is purely classical without kinetic corrections. Bohm boundary conditions are set on targets. Cross-field transport is assumed to be anomalous, with the transport coefficients being prescribed. Drifts and volume recombination are not yet included. Neutral gas is treated kinetically by the Eirene code. Global particle balance is self-sustained by assuming 100% recycling on the relevant plasma-facing components, without pumping and external particle sources.

Fig.2: SDC configurations with and without island control coil. With full control coil current the inner separatrix is shifted inwards and the two outer separatrices touching the targets are moved towards the divertor gap.

Hydrogen plasma is assumed, with carbon as a representative impurity species. The total power entering the SOL, P_{SOL}, is fixed to be 10 MW. The same cross-field diffusivity D is assumed for hydrogen and carbon and is varied in the range from 0.5 to 1m^2/s based on W7-AS experience. Cross-field heat conductivities for electrons and ions, χ_e and χ_i, are coupled with D as $\chi_e = \chi_i = 3 \times D$. Detachment is investigated in a plasma separatrix density range from 3 to 6×10^{19} m^{-3} and the total radiated power is used as a control parameter. Carbon atoms are started from targets according to the deposition distribution of the background hydrogen ions, with the yield controlled by the total radiation power. As a neighbor in the periodic table, nitrogen has a similar cooling property to carbon. Thus, the results obtained with carbon should, to a large extent, be valid for nitrogen, provided there is no restriction in the nitrogen gas inlet. Gas inlet optimization for impurity seeding is an important topic for the future.

For the reasons given in section 2, we restrict our studies to the high-mirror configuration bounded by the 5/5 island chain. Equilibrium is calculated using VMEC [36] +Extender [37] for $<\beta>\sim 3\%$. Vacuum SDCs (see figures 1 and 2) are used as reference.

The main drawbacks of the radiation thermal power dispersal concept via light impurities are the resulting core contamination and the consequent reduction of the recycling flux. Here, while increasing radiation, we monitor the carbon density/concentration at the LCFS and the neutral density/pressure in the unpumped divertor chamber. High radiation fraction, low carbon concentration and high neutral pressure are the criteria used for assessing the divertor plasma performance.

4. Role of external perturbation

Stable detachment on W7-AS was accessible only with help of the island control coils which amplified the resonant radial field b_r and increased the island size [20]. Stabilizing detached plasmas in LHD necessitates an external 1/1 perturbation field [19]. Although the underlying physics could differ from device to device, the experimental findings on W7-AS and LHD stimulate a closer look at this issue for W7-X.

A small, but finite resonant radial field component b_r (normalized to the total field strength) of the order of 10^{-3} is essential for the islands to act as divertor to guide plasma via fast parallel transport to targets which are positioned a certain radial distance away from the confinement region. Here, b_r determines the radial projection of parallel transport and thereby controls the relative weight to cross-field transport contributions. It is expected that the islands will lose their divertor function when b_r is so weak that parallel transport processes do not actually contribute to the plasma transport across the edge islands. This is certainly an extreme case. Another extreme case is known from the poloidal field divertor of tokamaks where the SOL plasma is diverted by a much stronger poloidal field component of the order of 10^{-1} and parallel transport dominates. In reality, the island divertor is situated somewhere in
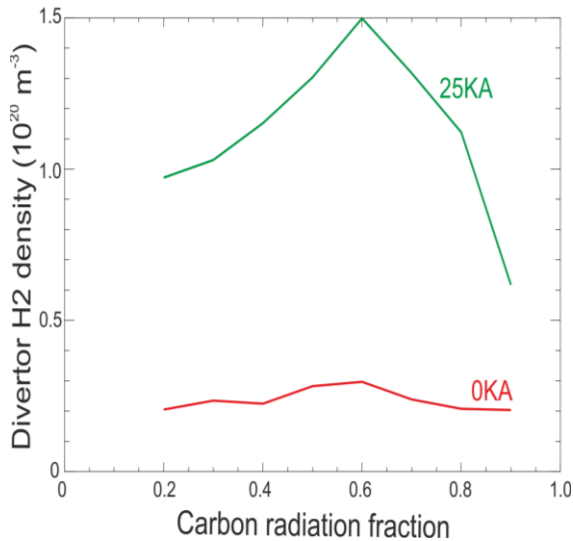

Fig.3: Hydrogen molecule density in the divertor chamber as functions of carbon radiation fraction for the $I_{cc}=0$ and 25 kA cases, respectively, with $D=0.5 m^2/s$, $n_{es}=6\times10^{19} m^{-3}$ and $P_{SOL} = 10MW$.
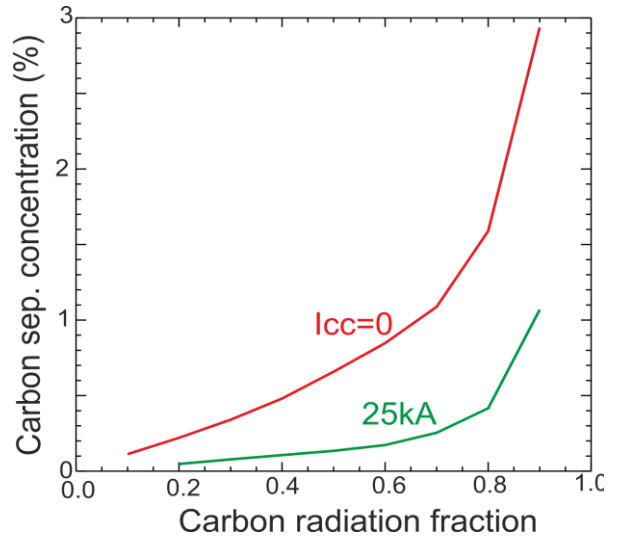
Fig.4: Carbon separatrix concentration versus carbon radiation fraction for the two cases with ($I_{cc}=25kA$) and without ($I_{cc}=0$) control coil current with the input parameters as for figure 3.

between where cross-field and parallel transport compete. Depending on the actual SOL plasma conditions, different transport channels have different parallel-to-perpendicular transport ratios which vary from place to place inside the island SOL and can be externally controlled by b_r, making the island divertor more interesting. A more detailed description of the essential transport features of the W7-AS divertor can be found in [29, 38] and a comparison between stellarator and tokamak divertor transport is made in [29, 30].

In general, increasing b_r increases the weight of parallel transport, bringing the island divertor transport characteristics closer to those of the conventional tokamak divertor [30]. A significant increase of the divertor neutral pressure by increasing b_r through the island control coils is shown in figure 3. There are different factors contributing to the significant rise in n_{H2} for the case with full control coil current I_{cc}. First, the strike lines for the $I_{cc}=25kA$ configuration are located closer to the divertor gap, as seen in figure 2. Second, the particle deposition is more focused in the poloidal direction and, third, the recycling flux is enhanced following a rise in target density [30]. The rollover of the divertor n_{H2} with carbon radiation fraction, particularly for the $I_{cc}=25kA$ configuration, will be discussed later.

The impact of the external perturbation fields on the carbon impurity is shown in figure 4. After switching on control coils with full I_{cc}, the carbon concentration at the LCFS needed for achieving a same amount of radiation is reduced by a factor of 3-5 depending on the radiation strength. Two major effects contribute to this reduction of the carbon concentration at the LCFS. First, a larger b_r raises the plasma density in the radiation zone for the same reason as stated for the rise of the target density [30]. Second, under certain SOL plasma conditions increasing b_r improves the retention effect of the edge islands on intrinsic impurities.

The first systematic EMC3-Eirene studies of impurity transport in a 3D helical SOL were made for the W7-AS island divertor where a retention effect on intrinsic impurities at high SOL collisionalities was identified and explained [29]. More precisely, a SOL impurity transport regime was identified in which the classical ion thermal force is strongly suppressed in favor of the flushing-out action of the background ion flow by means of impurity-ion friction. This favorable regime is accessible for SOLs where the diverting fields are sufficiently weak. Recently, dedicated numerical and experimental studies of this issue have been carried out for the LHD helical divertor [39, 40, 41]. In what follows we give a brief explanation of the physics of this regime, with details being described in [30].

Within the trace impurity limit and fluid approach, the dominating classical forces acting on impurity ions are the ion thermal and friction force. Both forces arise from ion-impurity collisions. The bulk ion flow in the island SOL has always an outward-directed radial component and tends to push impurities outward. Local flow reversal effects, as discussed in the tokamak literature (s. Chapter 5 in [26] and the references therein), have not been seen in the island divertor, neither numerically nor experimentally. In contrast, the ion thermal force, which results from the parallel T_i-gradient and is directed opposite to the parallel ion heat flux, drives impurities upstream toward the heat origin, i.e. the inner separatrix. The impurity flow direction is determined by the competition resulting between the ion friction and thermal force. It can be shown that the ion thermal force is associated with the ion conductive heat flux and the condition for the friction force to dominate over the thermal force is that the convective ion heat flux exceeds the conductive one [42]. In general, this

condition is satisfied in the near-target region where the ion Mach number exceeds a certain value [43], constrained by Bohm boundary conditions. In most of the SOL region of tokamaks, parallel heat conduction governs the ion energy transport, leading to an impurity density build-up at the inner separatrix. In stellarators, b_r is so small that cross-field heat conduction can significantly contribute to the ion heat transport across the islands and thereby reduce the parallel ion heat flux and the related ion thermal force. The former dominates over the latter when $\chi_{i\perp} n_i > b_r^2 \kappa_i T_i^{5/2}$ where κ_i is the Spitzer heat conduction coefficient. Once this condition is approached at the inner separatrix, the parallel ion heat conduction channel is blocked throughout the island SOL because of the high T_i-sensitivity of the classical heat conductivity. As a consequence, the related ion thermal force is reduced in favour of the friction force. Under this constraint, increasing b_r increases the radial impurity outflow velocity, enhancing the impurity retention effect of the edge islands.

5. Island size effects

W7-AS divertor experiments have shown that a sufficiently large island is necessary for stabilizing detachment [16, 20, 28]. Limited by the small machine size of W7-AS, the maximum radial width of the 5/9 islands available even with help of the control coils was only about 4 cm. Here, a question remains: what is expected for larger islands? This question is not only scientific but also is of economic significance because the edge islands take up valuable space inside the vacuum vessel that could otherwise be used for confinement.

High-mirror configurations are selected in this study for the reasons given in section 2. The equilibrium for $<\beta>\sim3\%$ is calculated by the VMEC code, with the resulting B-fields being connected/extended to the SOL region using the Extender code. The island size is varied by applying the planar coils to shift the 5/5 resonance with respect to the targets, yielding three different configurations. Additionally, three vacuum SDCs with full I_{cc} are generated in an analogous way as reference for their relevance for studying the basic island
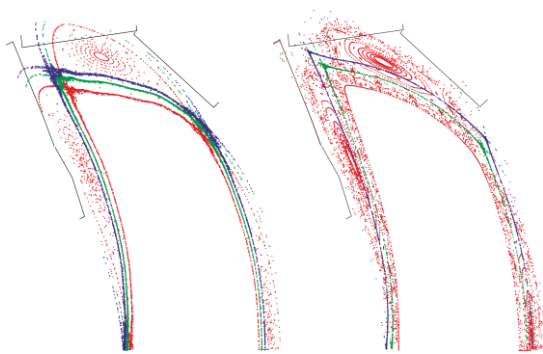

Fig.5: Configurations chosen for studying island size effects. Left, high mirror with $<\beta>\sim3\%$, calculated using VMEC+Extender. Right, vacuum SDC with full I_{cc} as reference. Island size is varied by applying planar coils, yielding 6 configurations in total.
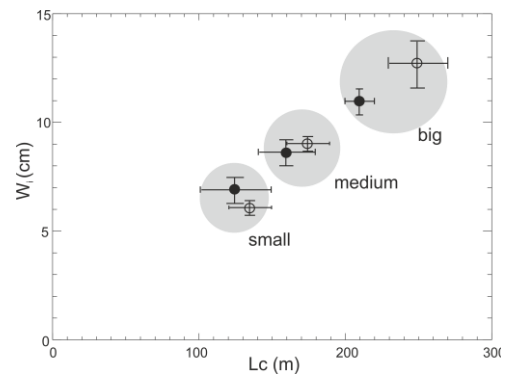

Fig. 6: Configurations are ordered by island width W_i and connection length L_c. High mirror configurations are indicated by solid circles, while the vacuum SDCs are denoted by open circles.

divertor physics. Figure 5 shows the resulting divertor configurations, which are ordered by the island width W_i and the connection length L_c in figure 6. Here, W_i and L_c are determined

in a cylindrical approximation of the plasma volume filled with reasonably large L_c. Details of this procedure can be found in the Appendix. To facilitate the discussion, the 6 configurations are divided into three groups according to their size, and are termed as small, medium and big island, respectively, as indicated in figure 6. Each group consists of one high-mirror configuration and one SDC for comparison.

Calculations for the 6 selected configurations are performed under the same conditions of $P_{SOL}=10MW$, $n_{es}=6\times10^{19}$ m^{-3} and D=0.5 m^2/s and for respective radiation fractions of 60%, 80% and 90%. Figure 7 shows the carbon concentrations at the LCFS needed for each configuration to reach the desired respective radiation strengths. The dashed curves are introduced just for guiding the eye. Higher carbon concentration is needed for higher radiation, explaining why the curves in figure 7 shift upward with increasing radiation fraction. In spite of their different locations, the three curves exhibit a common feature, namely that the carbon concentration has a minimum around the medium-sized islands.
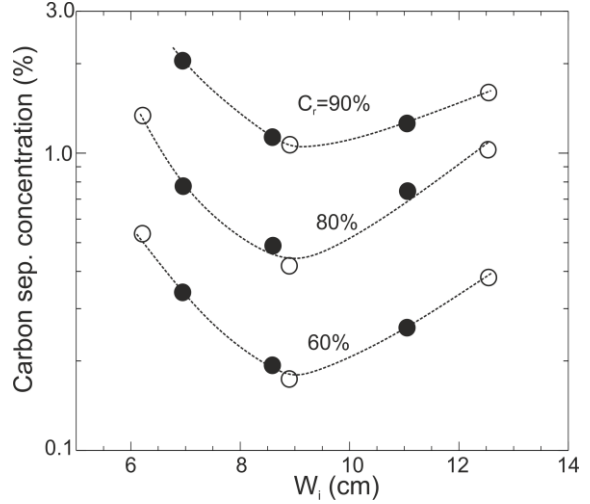

Fig.7: Carbon concentration at the LCFS as function of island width for three radiation fraction values of 60%, 80% and 90%. The circles have the same meaning as in figure 6. Dashed curves guide the eye.

It has been found that the medium-sized islands are optimum for neutral compression, too. Figures 8 and 9 show the maximum molecule pressure P_0 achieved in the divertor chamber as a function of radiation fraction for the respective high-mirror configurations and SDCs. Molecules are re-emitted from the in-divertor-chamber wall and plate surfaces, for which the room temperature of 300K is assumed. Contributions from energetic hydrogen
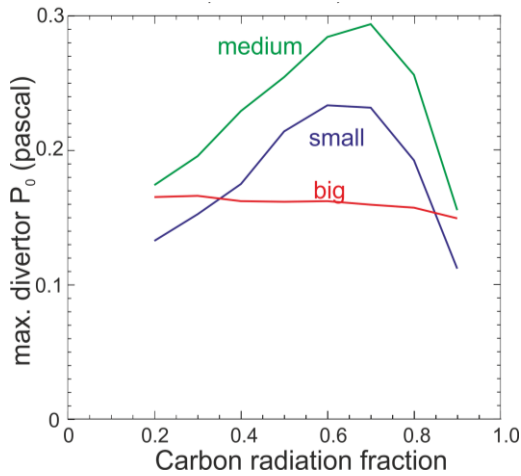

Fig. 8: neutral pressure in the divertor chamber as function of carbon radiation fraction for high-mirror configurations.
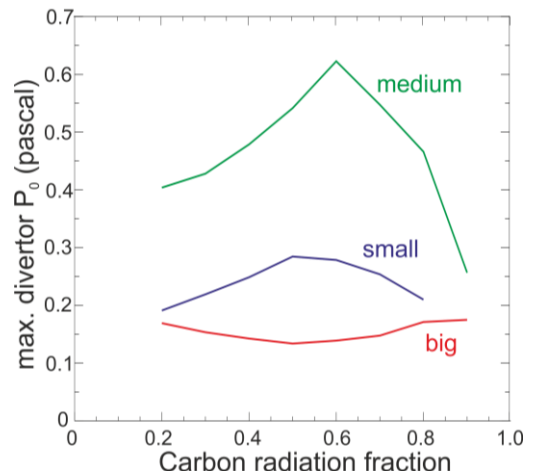

Fig. 9: neutral pressure in the divertor chamber as function of carbon radiation fraction for SDC configurations

atoms are not taken into account because they are less relevant for neutral pressure measurements and particle pumping. Despite the differences in the absolute P_0 values between the high-mirror and SDCs, mainly due to different strike line locations, figure 8 and 9 show coincidently that the highest P_0 is achieved for the respective medium-sized islands. In addition, the results show similar dependences of P_0 on carbon radiation fraction between the high-mirror and SDC islands within each group. For the small and medium islands, both the SDC and high-mirror configurations show that P_0 initially increases with radiation, reaches a maximum and then drops. In contrast, P_0 for the large island is insensitive to radiation. These results imply that the neutral behavior is largely determined by the island topology characterized by e.g. W_i and L_c, rather than the source origin of the recycling neutrals associated with the strike-line location. The P_0 roll-over effect found in the small and medium islands will be discussed in the next section.

To understand the numerical results shown in figure 7, 8 and 9, we first need to have a close look at the carbon radiation distributions, which are shown in figure 10 for the case of
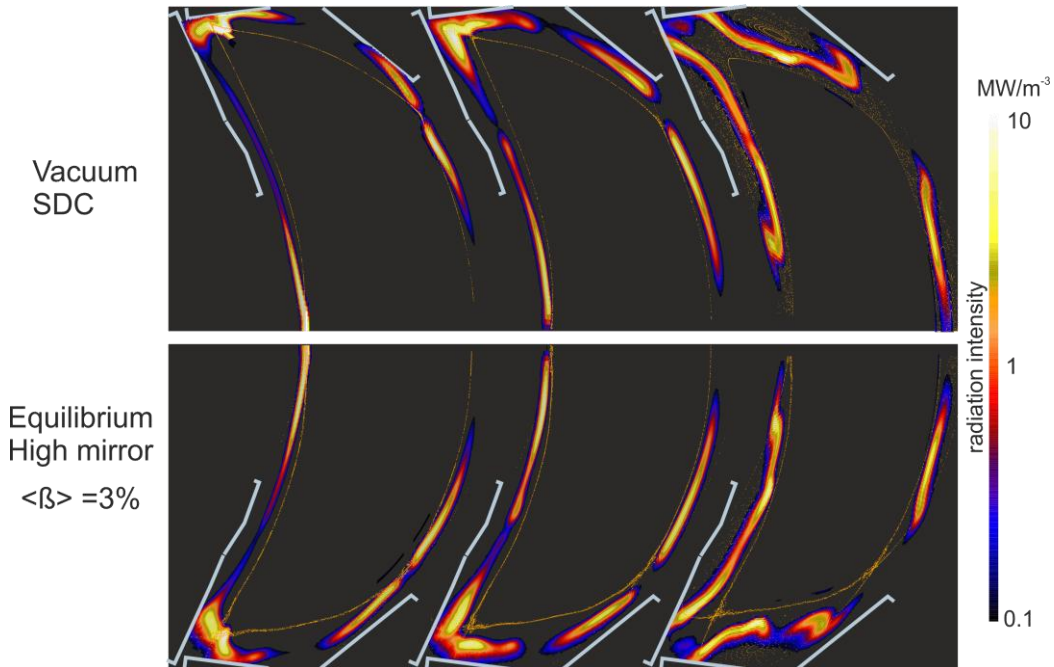

Fig. 10: Carbon radiation distributions for all the 6 selected configurations for the 80% radiation fraction case shown in figure 7. Top: SDCs; Bottom: high mirror configurations. Island size increases from left to right.

80% radiation fraction depicted in figure 7. The SDC and high-mirror configurations are plotted in a bean-shaped plane in a paired, mirror manner, with island growing from left to right. Only a half of the bean-shape plane is shown for each because the computations preserve the stellarator symmetry of W7-X. At first glance we see more in-out-symmetric radiation distributions than those for W7-AS, where the calculated carbon radiation is mainly located around the X-points on the inboard side because of flux expansion effects [20]. Second, we see similar radiation patterns and even similar absolute radiation strengths between the respectively up/down-paired SDC and high-mirror configurations of comparable W_i and L_c (s. figure 6) despite the different strike-line locations (s. figure 5). These results once again demonstrate the leading roles of W_i and L_c in determining the essential island

divertor transport features, and confirm the relevance of using vacuum configurations for studying the basic island divertor physics. Third, there are two different radiation patterns, i.e. radiation around X-points for the small and medium islands and radiation surrounding islands for the big ones.

The island divertor needs a finite island width W_i. One would reasonably expect that the island divertor will degrade down to a limiter when $W_i \rightarrow 0$. This serves as an intuitive explanation for why the small islands exhibit a worse performance in terms of impurity retention and neutral compression, without requiring further justification. Now, we turn our attention to the big islands. In contrast to the small and medium islands, the big islands are not fully opened by the targets, but leave a remnant island core around the O-point, which can be clearly seen in the Poincare plots shown in figure 11. Zooming into the divertor region, the difference between the two radiation patterns becomes more apparent. One clearly sees a radiation belt surrounding the remnant core of the big island, while an intensive radiation zone appears around the X-point(s) for the medium-sized island. The island-surrounding radiation belt cools the whole big island, making the geometrically big island "optically" thin for the impurity and recycling neutrals.
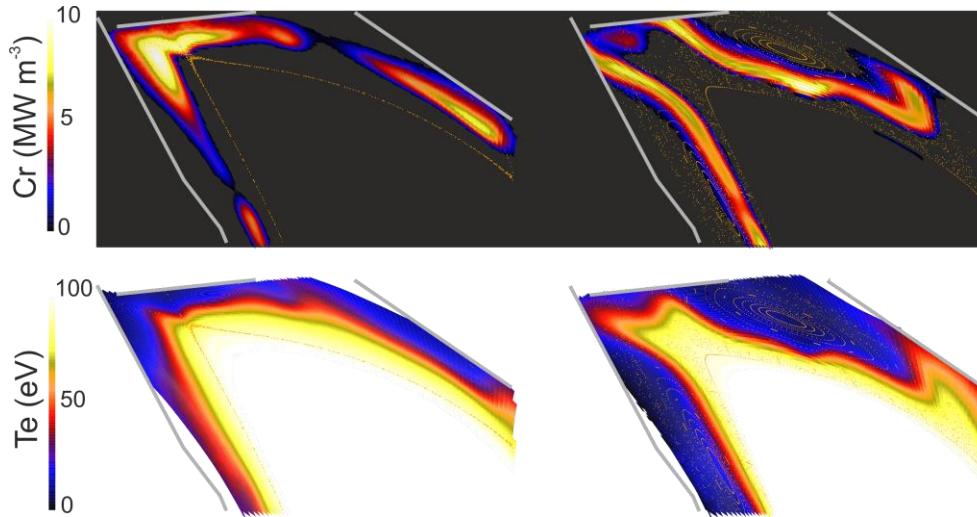
Fig. 11: Zoomed radiation contours (top) and T_e-distributions (bottom) for the medium (left) and big (right) SDC islands. The medium island is only for reference.

The remnant island core is the most likely candidate responsible for the formation of the island-surrounding radiation band. In fact, island cooling-down processes start already before intensive impurity radiation. Directly exposed to the recycling neutrals of a huge flux, the island core is fed sufficiently to result in a significant density buildup because of the absence of parallel loss channels. Within the fluid model adopted in EMC3, particles (ions and electrons) leave this "sub-confinement region" via cross-field diffusion. The associated convective heat flux and the power lost in ionization processes cool the island core. As a consequence, the island is too cold for impurity radiation and, instead, more favorable radiation conditions are found in the periphery of the big island in contact with the main power channel. Impurity radiation cools the island further, easing the penetration of the carbon and recycling neutrals across the island to sustain the island surrounding radiation pattern. If this is true, the radiation pattern should change, presumably to the X-points, after

fully opening the islands in some manner. Generally, the perturbation fields either from the 3D coils or the island control coils drop rapidly when shifting the resonance inward to obtain a bigger island, however. While the question of how to completely open a big island remains unanswered, we make a concluding point here, i.e. that a closed remnant island core of a confinement-relevant size is unfavorable for detachment operation of the island divertor.

6. Radiation limitation and compromise between particle and power exhaust

In this section, we discuss some critical issues that potentially restrict the radiation power removal capability of the edge islands. The simulations show a general tendency that the radiation layer moves inward with rising radiation, independently of configuration. Nevertheless, at what radiation strength the radiation layer reaches the LCFS does depend on the island width. For instance, at 80% radiation the radiation front in the small islands has already intruded into the confinement region (see figure 10), while for the medium and big islands

Fig. 12: Dependences of carbon concentration at the LCFS and divertor neutral pressure on carbon radiation fraction for the high-mirror medium island.

radiation takes place on open field lines outside the LCFS. It has been found that, even at a radiation level of 90%, the radiation layers for the medium and big islands are still located outside the LCFS. In contrast, detachment simulations made for W7-AS never produced an island radiation fraction of more than 80%. Any attempt with stronger radiation in simulation always leads to formation of an intensive, "Marfe'-like radiation zone inside the LCFS around the inboard mid-plane. Benefiting from the more in-out-symmetric flux surface geometry, the W7-X islands potentially allow for more power to be radiated on open field lines, which is indicated by modeling. In simulations, the SOL plasma is isolated from the core plasma in such a way that P_{SOL}, n_{es} and the total radiation power are fixed. In experiments simultaneous control of these parameters is difficult. Thus, in reality, there could be many factors which can affect the stability of an intensively radiating plasma and restrict the actual radiation capability of the edge islands.

Using the high-mirror medium island as example, figure 12 shows how the carbon concentration at the LCFS and the neutral pressure in the divertor chamber respond to the
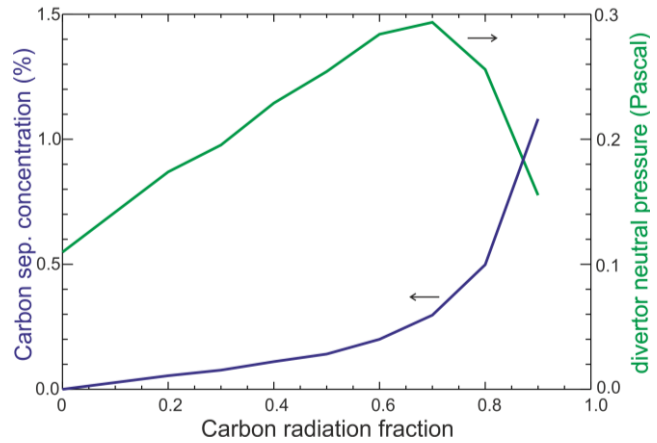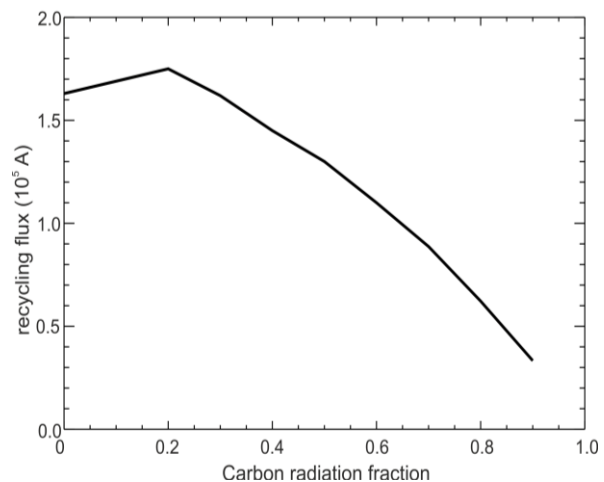

Fig. 13: Total recycling flux as a function of carbon radiation fraction for the high-mirror medium island.

variation of radiation. The other code input parameters are fixed. Up to a radiation fraction of 70%, radiation increases the neutral pressure in the divertor chamber. After that, the neutral pressure drops even faster at higher radiation strengths. Simultaneously, the carbon concentration at the LCFS grows rapidly. In steady-state operation, active pumps installed inside the divertor chambers would be the only particle sinks. In this case, a drop in the neutral pressure reduces the pumping rate, consequently leading to loss of density control.

The drastic changes of the neutral pressure and the carbon concentration in the high radiation range are associated with an inward movement of the radiation layer across the island. Intensive radiation causes "plasma condensation" characterized by low temperature and high density. This also happens to impurities because of the dominating ion-impurity friction force under such high-collisionality conditions. With the radiation layer/condensation zone approaching the separatrix, the impurity density at the LCFS increases due to the anomalous diffusive process assumed in the fluid model.

The roll-over of the divertor neutral pressure with rising radiation in figure 12 is driven by a combined effect of recycling and neutral penetration associated with the specific divertor geometry. Figure 13 shows the evolution of the recycling flux (total bulk ion efflux onto targets) with increasing radiation. The recycling flux reaches a maximum at a radiation fraction of 20% and then drops. A coincident roll-over is also observed for the target plasma density. In divertor experiments roll-over of the ion saturation current is a sign for onset of detachment, happening for carbon machines usually at higher radiation fractions. The earlier onset of roll-over of the recycling flux shown in figure 13 is due to the high separatrix density (6×10^{19} m^{-3}) assumed in the computations. In tokamaks, a reduction of the ion saturation current in detachment is mainly caused by momentum losses from neutral-plasma friction and further strengthened by the subsequent volume recombination processes. In the simulations made here for W7-X, volume recombination processes are not included and the drop of the recycling shown in figure 13 is mainly driven by momentum losses and flow channel broadening effects induced by cross-field transport processes associated with the 3D island geometry and the long connection lengths. The drop of the divertor neutral pressure P_0 in the high radiation range is a consequence of the decrease of the recycling flux in that range. What is then the reason for the continuous rise of P_0 before, when the recycling flux already falls? To understand this point we need to have a look at the plasma-surface interaction situation for the high-mirror medium island shown in figure 5. The strike lines are located over a certain distance away from the divertor gap. It has been found that the neutrals entering the divertor chamber are predominantly atoms resulting from charge-exchange and Franck-Condon dissociation processes. In the absence of impurity radiation, the plasma at the targets is "optically" thick and most of the atoms are trapped around the strike lines within a thin layer in front of the targets. Radiation lowers the temperatures at the targets, increasing the ionization lengths of the atoms and easing their penetration toward the divertor gap. This effect over-compensates the drop of the recycling flux and remains effective as long as the neutral penetration length is smaller than the mean distance of the atoms to the divertor gap. Once the two characteristic lengths become comparable, this "optical"-depth effect will be saturated and the recycling flux will take over the leading role in determining the neutral pressure in the unpumped divertor chamber. It is interesting to see that the maximum neutral

pressure is achieved at an interestingly high radiation level, showing a good compatibility between particle and energy exhaust.

It should be mentioned that EMC3-Eirene simulations for W7-AS have shown a similar radiation-dependence of the divertor chamber neutral pressure, despite some differences in detail. In the divertor experiments on W7-AS, a significant rise in P_0 after detachment transition is indeed observed, nevertheless only in one of an up-down divertor chamber pair instrumented with neutral gauges [27]. Depending on the B-field direction, once the plasma goes into detachment, the neutral pressure in one divertor chamber increases typically by a factor of 3-5, while staying constant or even marginally decreasing in the other. For the divertor module where P_0 significantly rises, spectrometers measure a high ratio of H_γ and H_α emission lines originating from the near-target region, indicating the existence of a localized recombination zone [44, 45]. The interplay between P_0 and volume recombination is still unclear. Volume recombination processes are not included in the EMC3-Eirene code. An estimate by post-processing the 3D simulation results for W7-AS shows a negligible role of volume recombination in comparison with surface recombination processes, however. To more deeply understand these issues, classical drift effects, which are numerically not yet accessible, must be taken into account. In fact, the observed correlation of the up-down asymmetry in P_0 with field direction has pointed to such effects.
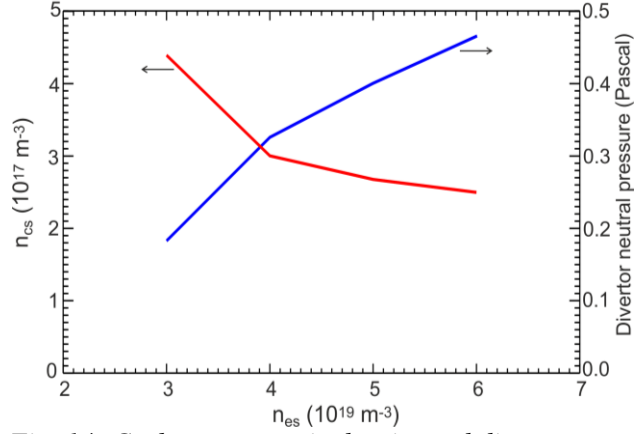

Fig. 14: Carbon separatrix density and divertor neutral pressure as functions of n_{es} for the medium SDC island with fixed radiation fraction of 80%.
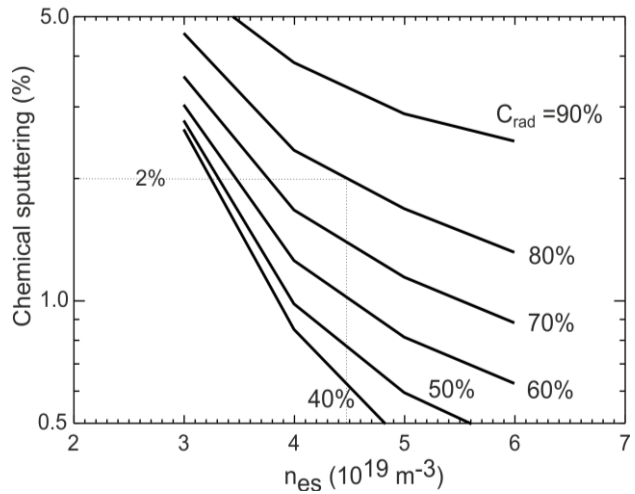
Fig. 15: Correlations of radiation fraction, sputtering coefficient and n_{es} for the medium SDC island. In a carbon machine like W7-X, radiation is function of n_{es} depending on the actual chemical sputtering coefficients. Physical sputtering is irrelevant under the divertor plasma conditions of

7. Favorable operational density range

All the results shown in the previous sections are calculated with a relatively high separatrix density of 6×10^{19} m^{-3} - the highest separatrix density ever observed in W7-AS experiments. As the radiation intensity is proportional to the electron and impurity density, it

is reasonable to expect that a smaller impurity fraction would be required when the plasma is operated at higher plasma densities. This is indeed confirmed by the 3D simulations. Using the SDC medium island as example, figure 14 shows how the carbon separatrix density needed for achieving the same amount of radiation of 8 MW decreases with increasing operational plasma density, where n_{cs} decreases with n_{es} roughly as $1/n_{es}$. In addition, figure 14 shows another beneficial effect, i.e. that the divertor neutral pressure increases with rising n_{es}, even stronger than linearly. Under such high radiation conditions (80%), the total recycling flux is rather insensitive to n_{es}, having increased by ~20% after n_{es} is doubled. Thus, there must be other reasons for the more than factor-of-2 increase in the neutral pressure. At present, the most plausible explanation is that a higher density will reduce the neutral penetration length across the radiation layer. In the cold, dense radiation layer, charge-exchange is the main reaction process. There, the CX-neutrals undergo a diffusion-like process. Higher plasma densities increase the CX-reaction rates and thereby decrease the "diffusivity". To some extent the radiation layer acts as a "diffusion barrier" for the cold neutrals behind it.

So far, the plasma separatrix density and the total radiation power are regarded as independent control parameters. This assumption is reasonable only for extrinsic impurities. For a carbon machine like W7-X in the initial phase, carbon radiation and n_{es} correlate with each other. In this case, n_{es} can be restricted by carbon radiation. Figure 15 shows the n_{es}-values needed for achieving different radiation fractions with assumption of different chemical sputtering coefficient values, which are varied by one order of magnitude to account for uncertainties in plasma-surface interaction processes. Assuming 2% chemical sputtering, 80% radiation needs a n_{es}-value of about 4.5×10^{19} m^{-3}. Thus, an investigation of detachment performance at higher n_{es} is possible only with a metal divertor - probably tungsten in a later phase.

8. Island neutral screening effect

Most of the recycling neutrals are ionized inside the islands. Only a small portion of them can reach the confinement core and be ionized there. The total ionization source inside the confinement region depends on the island size, SOL and the core plasma parameters. For the
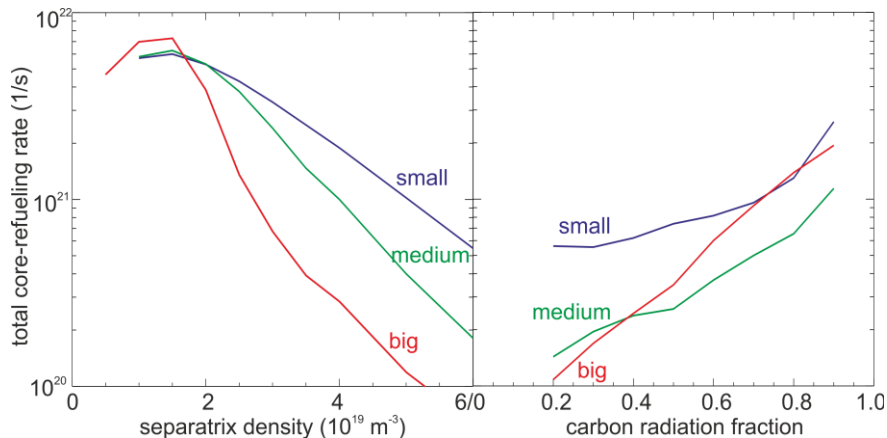

Fig. 16: Total refueling rate as function of n_{es} (left) and further as function of radiation fraction with n_{es} fixed to be $6 \times 10^{19} m^{-3}$.

three high-mirror configurations figure 16 shows the total core refueling rates as a function of n_{es} in the absence of impurity radiation and further as a function of the radiation fraction with fixed $n_{es} = 6\times10^{19}$ m^{-3}. Core temperature profiles are calculated by the NTSS code [46] assuming neo-classical transport for the central region and anomalous transport at the edge. The core density profile is prescribed. In the high n_{es} range of interest, all three refueling rate curves drop with increasing n_{es} due to the improved screening effect of the edge islands on the recycling neutrals and the bigger the islands, the stronger the screening effect. Note that, in this n_{es}-range, the recycling flux for all the three configurations increases continuously. In the presence of impurity radiation, the refueling rates recover to some extent due to temperature effects, depending on the island size and the corresponding radiation pattern. In general, increasing the radiation during detachment leads to an inward movement of the ionization front and reduces the effective "optical" thickness of the edge islands. Here, the radiation distribution plays an important role. Recall the argument for the divertor performance degradation in terms of neutral gas compression of the big islands in section 5, i.e. that the island-surrounding radiation pattern makes the big island "optically" thin. This is indeed confirmed in figure 16, where the refueling rate of the big island increases more quickly than the others and exceeds that of the medium island in the high radiation range.

The lack of knowledge concerning anomalous transport coefficients at the edge means that we do not yet know the actual particle source required to establish a desired core density in W7-X. Nevertheless, simulations for the much smaller W7-AS under detachment conditions yield a typical refueling rate in the range of 2-4$\times10^{21}$/s [29] – a number which is even larger than that produced for the W7-X divertor configuration and plasma parameter range of interest. Note the large difference in machine size between W7-AS and W7-X. Thus, it is concluded that, for the most interesting divertor configurations and plasma parameters in W7-X, the recycling neutrals do not provide a sufficient particle source for the confined core. The consequences are twofold. On the one hand, the SOL divertor plasma is more isolated from the core plasma in the sense that any perturbation and change originating in the SOL cannot propagate into the core by means of the recycling neutrals. In contrast, the SOL plasma in W7-AS was strongly coupled with the core via the recycling neutrals, which could drive detachment instabilities under certain conditions [20]. On the other hand, for controlling the core plasma density, central particle fueling is necessary. Pumping out the externally injected particles to keep the plasma in steady state presents a big challenge for the island divertor of W7-X, however.

9. Conclusions

W7-X island divertor performance under detachment conditions has been explored using the EMC3-Eirene code. High radiation fraction, low impurity density at the last closed flux surface and high neutral pressure in the divertor chamber are the criteria used for assessing the island divertor performance. Optimal conditions are explored in both configuration and plasma parameter space. Numerical results indicate that there is an optimum island size for reducing the impurity density at the separatrix and for increasing the neutral pressure in the divertor chamber. For fully-opened islands, radiation is located around the X-points. In this case, increasing the island size improves the "optical" thickness of the island SOL. Bigger

islands with a remnant closed core of a confinement-relevant size lead to formation of a radiation belt surrounding the islands which cools down the islands and reduces their "optical" thickness.

It is also shown that a stronger diverting field b_r improves the island divertor performance in terms of impurity screening and neutral compression. A factor-of-2 increase in b_r via island control coils leads to a decrease of the carbon separatrix density by a factor of 3-5 and a rise of the neutral pressure in the divertor chamber by a factor of 3-6, depending on the radiation strength. These favorable effects are attributed to the increased efficacy of parallel transport processes, provided that the SOL plasma is operated in the ion-friction-dominating impurity transport regime at high SOL densities.

It is found that, for the specific island divertor geometry, appropriate impurity radiation eases the penetration of the recycling neutrals into the divertor chamber. For the divertor configurations of interest, the highest neutral pressure is achieved at a radiation fraction of 60-70%, showing a good compatibility between particle and energy exhaust up to this point. At higher radiation levels, another effect, i.e. that the recycling flux decreases with radiation, becomes dominant and the neutral divertor pressure falls with slope steepening at radiation fractions of more than 80%. Meanwhile, the separatrix impurity density rises sharply and is accompanied by a rapid inward movement of the radiation layer toward the inner separatrix. Loss of density control and a subsequent inward shift of the radiation layer into the confinement region could result and restrict the radiation power removal capability of the edge islands.

High SOL plasma density is favorable for detachment operation. Simulations show that fewer impurities will be needed and higher neutral pressure can be achieved when detached plasmas are operated at higher plasma densities. Unfortunately, for a carbon machine like W7-X in the initial phase, the maximum operational density is limited by intrinsic carbon radiation. This limit can be relaxed later by installing a tungsten divertor.

For the most interesting divertor configurations and SOL plasma parameters, the island SOL in W7-X is almost "opaque" for the recycling neutrals in the sense that they cannot really reach and refuel the core plasma. This offers a possibility for the core plasma density to be controlled independently, necessitating additional particle central fueling of course, and thereby presenting a challenge for the island divertor to exhaust these externally-injected particles.

Acknowledgements

Appendix. Definition of island width W_i and L_c

The radial island width W_i and the target-to-target connection length L_c are two important geometric parameters which determine the characteristic perpendicular and parallel transport length scales of the island divertor. In reality, W_i and L_c are 3D parameters varying significantly from place to place, as can be seen in the top picture of figure A1. Note that the form of the cross-section changes in the toroidal direction. In section 5, however, they are used as global parameters for ordering the divertor configurations in some average sense. Here, we explain these averages and how they are determined.

We start with a calculation of the plasma volume filled with field lines of sufficiently large connection lengths as

$$V(L_{low}) = \int_{L_c > L_{low}}^{\infty} dV \qquad (A.1)$$

where L_{low} is a free parameter which sets the lower boundary of a high-L_c-pass filter. We introduce an "effective" radius r_{eff} via a cylindrical approximation of $V(L_{low})$ and calculate r_{eff} by

$$2\pi^2 R \cdot r_{eff}^2 (L_{low}) = \int_{L_c > L_{low}}^{\infty} dV \qquad (A.2)$$

where R is the major radius and r_{eff} is a function of L_{low}. Using the SDC with full I_{cc} as example, figure A1 shows the L_{low}-dependence of r_{eff}. The regions behind the divertor plates have short connection lengths and are completely filtered out when L_{low} is increased to ~30 m. The $L_c = L_{low} = 30$ m contour line is dashed in the top picture of figure A1. From this point on, the L_{low} contour line shrinks first in the private flux regions between two neighboring islands, leading to a flattening of the r_{eff}-curve with respect to L_{low}, and then enters the island SOL of long-L_c, causing a drastic drop of r_{eff}. Depending on whether the private flux regions are taken into account, the
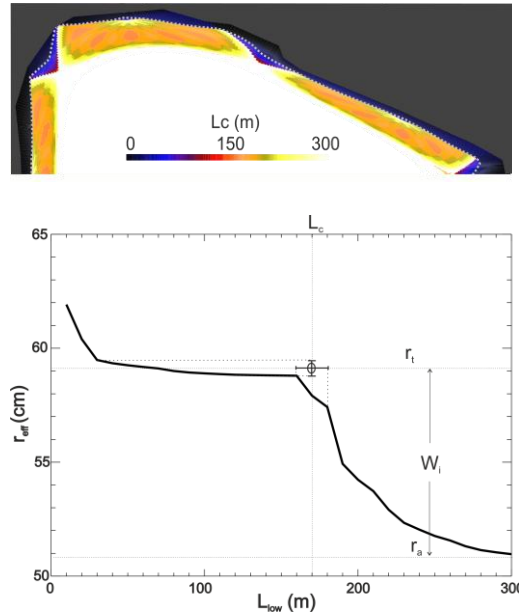

Fig. A1: L_c distribution of the vacuum SDC 5/5 island chain with full I_{cc} on the upper half of an up/down symmetric triangular plane (top) and "effective" radii of plasma volume as function of L_{low} – the lower boundary of a high-L_c-pass filter (bottom).

r_{eff}-coordinate of the target, r_t, can be determined either at the first kink point of the r_{eff}-curve, or at the second one after which r_{eff} falls drastically. In this paper, we take the average value between the two kink points, and define the L_c around the second kink point as the characteristic connection length of the islands, as shown in figure A1. The position of the LCFS, r_a, can be calculated by eq (A2) by setting $L_{low} \to \infty$ for completely-open islands or independently determined from the core side otherwise. Then, the radial island width is given by $W_i = r_t - r_a$.

References

[1] Zohm H. *et al* 2013 *Nucl. Fusion* **53** 073019

[2] Loarte A. *et al* 2007 *Nucl. Fusion* **47** S203

[3] Tobita K. *et al* 2009 *Nucl. Fusion* **49** 075019

[4] Eich T. *et al* 2011 Phys. Rev. Lett. **107** 215001

[5] Goldston R. 2012 *Nucl. Fusion* **52** 013009

[6] Beidler C.D. *et al* 1996 16th FEC, *Fusion Energy 1996* **Vol.3** 407
   http://www-naweb.iaea.org/napc/physics/FEC/STIPUB1004_VOL3.pdf

[7] Feng Y. 2013 *J. Nucl. Mater.* **438** (suppl.) S497

[8] Kallenbach A. *et al* 2013 *Nucl. Fusion* **55** 124041

[9] Pacher G. 2007 *Nucl. Fusion* **47** 469

[10] Asakura N. *et al* 1996 *Nucl. Fusion* **36** 795

[11] Petrie T. W. *et al* 1997 *Nucl. Fusion* **37** 321

[12] Pitcher C. S. and Stangeby P. C. 1997 *Plasma Phys. Control. Fusion* **39** 779

[13] Grigull P. *et al* 2001 *Plasma Phys. Control. Fusion* **43** A175

[14] Renner H. *et al* 2002 *Plasma Phys. Control. Fusion* **44** 1005

[15] König R. *et al* 2002 *Plasma Phys. Control. Fusion* **44** 2365

[16] Grigull P. *et al* 2003 *J. Nucl. Mater.* **313-316** 1287

[17] Evans T. *et al* 2004 *Phys. Rev. Lett.* **92** 235003

[18] Ohyabu N. *et al* 1994 *Nucl. Fusion* **34** 387

[19] Kobayashi M. 2010 *Physics of Plasmas* **17** 056111

[20] Feng Y. *et al* 2005 *Nucl. Fusion* **45** 89

[21] Wenzel U. *et al* 2002 *Plasma Phys. Control. Fusion* **44** L57

[22] Thomsen H. *et al* 2004 *Nucl. Fusion* **44** 820

[23] Baker D.R. *et al* 1982 *Nucl. Fusion* **22** 807

[24] Lipschultz B. *et al* 1984 *Nucl. Fusion* **24** 977

[25] Lipschultz B. *et al* 1987 *J. Nucl. Mater.* **145-147** 15

[26] Stangeby P. C. 2000 *The Plasma Boundary of Magnetic Fusion Devices (Plasma Physics Series)*(Bristol: Institute of Physics Publishing)

[27] McCormick K. *et al* 2005 *J. Nucl. Mater.* **337-339** 520

[28] Hirsch M. *et al* 2008 *Plasma Phys. Control. Fusion* **50** 053001

[29] Feng Y. *et al* 2006 *Nucl. Fusion* **46** 807

[30] Feng Y. *et al* 2011 *Plasma Phys. Control. Fusion* **53** 024009

[31] Geiger J. *et al* 2010 *Contrib. Plasma Phys.* **50** 770

[32] Turkin Yu. *et al* 2006 *Fusion Science and Technology* **50** 387

[33] Hölbe H. *et al* 2016 *Nucl. Fusion* **56** 026015

[34] Feng Y. *et al* 2004 *Contrib. Plasma Phys.* **44** 57

[35] Reiter D. et al, 2005 *Fusion Sci. Technol.* **47** 172

[36] Hirshmann S.P. and Whitson J.C. 1983 *Phys. Fluids* **26** 3553

[37] Drevlak M. 2005 *Nucl. Fusion* **45** 731

[38] Feng Y. *et al* 2002 *Plasma Phys. Control. Fusion* **44** 611

[39] Kobayashi M. *et al* 2013 *Nucl. Fusion* **53** 033011

[40] Chowdhuri M. B. *et al* 2009 *Phys. Plasma* **16** 062592

[41] Nakamura Y. *et al* 2014 *Plasma Phys. Control. Fusion* **56** 075014

[42] Krashenninikov S. I. *et al* 1991 *Nucl. Fusion* **31** 1455

[43] Neuhauser J. *et al* 1984 *Nucl. Fusion* **24**, 39

[44] Wenzel U. *et al* 2004 *Nucl. Fusion* **44** 1130

[45] Ramasubramanian N. *et al* 2004 *Nucl. Fusion* **44** 992

[46] Turkin Y., *et al* 2011 *Phys. Plasmas* **18** 022505